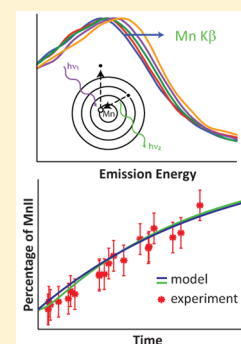


Kinetic Modeling of the X-ray-Induced Damage to a Metalloprotein

Katherine M. Davis,[†] Irina Kosheleva,[§] Robert W. Henning,[§] Gerald T. Seidler,[‡] and Yulia Pushkar*,[†][†]Department of Physics, Purdue University, West Lafayette, Indiana 47907, United States[‡]Department of Physics, University of Washington, Seattle, Washington 98195, United States[§]Center for Advanced Radiation Sources, The University of Chicago, Chicago, Illinois 60637, United States

S Supporting Information

ABSTRACT: It is well-known that biological samples undergo X-ray-induced degradation. One of the fastest occurring X-ray-induced processes involves redox modifications (reduction or oxidation) of redox-active cofactors in proteins. Here we analyze room-temperature data on the photoreduction of Mn ions in the oxygen-evolving complex (OEC) of photosystem II, one of the most radiation damage-sensitive proteins and a key constituent of natural photosynthesis in plants, green algae, and cyanobacteria. Time-resolved X-ray emission spectroscopy with wavelength-dispersive detection was used to collect data on the progression of X-ray-induced damage. A kinetic model was developed to fit experimental results, and the rate constant for the reduction of OEC Mn^{III} and Mn^{IV} ions by solvated electrons was determined. From this model, the possible kinetics of X-ray-induced damage at a variety of experimental conditions, such as different rates of dose deposition as well as different excitation wavelengths, can be inferred. We observed a trend of increasing dosage threshold prior to the onset of X-ray-induced damage with increasing rates of dose deposition. This trend suggests that experimentation with higher rates of dose deposition is beneficial for measurements of biological samples sensitive to radiation damage, particularly at pink beam and X-ray free electron laser sources.



INTRODUCTION

The high brilliance of third-generation X-ray synchrotron sources and newly constructed X-ray free electron lasers (FELs) allows for new types of measurements to analyze the structure and function of biological molecules.^{1–4} However, the associated increase in X-ray flux and rate of X-ray dose deposition exacerbates the problem of X-ray-induced damage to biological molecules and its effect on electronic and geometrical structures.

Here, we present an experimental and theoretical analysis of the X-ray-induced damage to the photosystem II (PSII) metalloprotein complex during exposure to the full flux achievable at a third-generation synchrotron source. PSII is an integral component of natural photosynthesis. The oxygen-evolving complex (OEC) of PSII contains a Mn₄Ca core. In the active protein, the Mn centers are present in both Mn^{IV} and Mn^{III} oxidation states. Earlier studies show that X-ray-induced damage to PSII manifests in the reduction of Mn centers to Mn^{II}^{5–8} and breakage of Mn di-μ-oxo units.^{7,8} To understand the origins of this effect, we review the stages of radiation damage known for biological specimens in the hard X-ray (5–15 keV) energy range, typical for protein crystallography and X-ray spectroscopy.

Primary damage is considered to arise from electrons generated in a cascade (on the time scale of tens of femtoseconds) after the interaction of X-rays with matter via absorption and inelastic scattering. The relaxation cascade eventually results in a large number of photoelectrons with energies of a few to several tens of electronvolts. The number and energy distribution of these electrons can be theoretically

estimated.⁹ Subsequent radiolytic reactions caused by products of primary damage are classified as secondary damage. The consequences of primary and secondary radiation damage reactions include the breakage of chemical bonds, generation of free radicals, and changes in the redox state of cofactors; these are commonly referred to as specific damage. In crystallography experiments, the alteration of individual biological molecules due to specific damage eventually causes long-range rearrangement of molecules in the crystal and a loss of crystalline order. This process is referred to as global damage. A number of experimental and modeling studies aimed at gaining a better understanding of the temporal and spatial progression of X-ray-induced damage in biological samples have been reported.^{10–18}

Temperature has a major effect on the rate of X-ray-induced damage. Experimentally, low temperatures (LTs) of 10–20 K drastically decrease the rate of X-ray-induced damage.^{5,6,12} Until recently,^{3,5,6,19–25} for PSII and other biological samples, cryogenic measurements have provided the only feasible method of data collection.^{8,26–28} Unfortunately, LT data collection is not applicable to dynamic studies of biological samples. Some transient intermediates can be trapped by freeze-quench and analyzed at LT; however, others, such as the proposed S₄ state in PSII, escape cryogenic trapping because of extremely short lifetimes. In such cases, time-resolved X-ray techniques (X-ray absorption spectroscopy, XAS, and X-ray emission spectroscopy, XES) remain the methods of choice as

Received: April 13, 2013

Revised: June 25, 2013

Published: July 1, 2013

they can characterize changes in the electronic structure over particularly short times.

Recently, we demonstrated a methodology allowing for room-temperature (RT) data collection capable of monitoring OEC state transitions with high time resolution.⁵ The high fluxes required to obtain experimental spectra make characterization and understanding of X-ray-induced damage to the OEC very important. Here, we use kinetic modeling to extract the rate of reaction of the OEC Mn core with free radicals generated in solution. The developed model can be further verified by analyzing damage kinetics observed with higher/lower rates of dose deposition as well as with the use of different excitation wavelengths.

MATERIALS AND METHODS

Experimental Methods. PSII-enriched thylakoid membrane particles were prepared from supermarket spinach.^{29,30} PSII was stored in a buffer using sucrose as a cryoprotectant: 0.4 M sucrose, 5 mM CaCl₂, 5 mM MgCl₂, 15 mM NaCl, and 50 mM MES, pH 6.0. The oxygen evolution activity of PSII was measured by a Clark-type electrode in a Hansatech oxygraph. The activity of the preparation was $\geq 300 \mu\text{mol of O}_2 \text{ (mg of Chl)}^{-1} \text{ h}^{-1}$ under constant saturating illumination at 25 °C utilizing 0.3 mM 2,6-dichloro-1,4-benzoquinone (DCBQ) as an artificial electron acceptor. The chlorophyll (Chl) *a:b* ratio was derived from the optical absorbance of chlorophyll extracted with an 80:20 acetone:water solution. This was measured with a Cary 300 Bio UV–visible spectrophotometer. For all samples, this ratio was $\leq 2.5:1$, indicating high enrichment of membrane particles with PSII. To ensure the high quality of the samples, LT X-band EPR spectra were recorded for the *S*₁ and *S*₂ states. *S*₂ state samples were obtained by illuminating *S*₁ state samples with a 120 W halogen lamp for 30 min while in a cold bath of ethanol and dry ice to maintain a sample temperature of 195 K, after which they were immediately frozen in liquid nitrogen. All sample preparation, handling, and storage environments were completely dark, save for dim green light when unavoidable, to prevent state transitions. In addition, samples were maintained at a constant temperature of approximately 4 °C during preparation. To simulate fully damaged PSII with 100% of Mn ions in the Mn^{II} oxidation state, a 100 mM MnCl₂ tetrahydrate stock solution was added to the PSII pellet samples. At the synchrotron radiation facility, the PSII samples for XES were prepared immediately prior to the measurements as follows: (i) After PSII stock preparations ($\sim 30 \text{ mg of Chl/mL}$) stored in liquid nitrogen were slowly thawed, the undiluted PSII pellet was spread onto polycarbonate holders with a 4 μm polypropylene tape backing stretched flat. (ii) The samples were then left to partially dry for $\sim 1.5 \text{ h}$ on ice under the flow of pure N₂. This ensured the highest PSII concentration possible in the beam.

X-ray emission spectra were collected at the Advanced Photon Source (APS) at Argonne National Laboratory on insertion device beamlines 20-ID and 14-ID (BioCARS). At sector 20, the radiation was monochromatized by a Si(111) double-crystal monochromator. Focusing was done using Rh-coated KB mirrors operated at 4 mrad grazing incidence. A He-filled chamber (*I*₀) with a beam cleanup pinhole was placed before the sample to monitor the intensity of the incident X-rays. The monochromator was calibrated via the KMnO₄ pre-edge located at 6543.3 eV. In addition, MnO emission spectra and Fe foil X-ray absorption near-edge spectroscopy measurements were taken periodically to monitor and correct for any

shift in energy calibration. To reduce the dose rate at 20-ID, a defocused mode was used with a $\sim 105 \times 85 \mu\text{m}^2$ projection of the beam onto the sample surface, 45° to the beam (angled to acquire the highest percent of analyzed fluorescence). A scan program synchronized with the shutter also provided sample protection from the beam during motor movements.

The BioCARS beamline provided a unique pulsed pink beam capability for XES experiments. The undulator gap and white beam slits¹ were set to give an undulator spectrum peaking at $\sim 7.85 \text{ keV}$ with a full width at half-maximum of $\sim 500 \text{ eV}$. To prevent unwanted fluorescence originating from the GaP spectrometer crystals, high-energy X-rays were suppressed by using the Si stripes of the KB mirrors with mirror angles of 3.8 mrad. The incident flux was monitored downstream of these mirrors via a photodiode. The high-heat-load chopper¹ was set to produce 44 μs pulses, and scans were synchronized with a pulse repetition rate of 41.1 Hz. Between pulses, all shutters were closed to save the sample from unnecessary degradation. The vertical mirror was defocused to give a final projection size of $\sim 50 \times 120 \mu\text{m}^2$ (*V* \times *H*) onto the sample surface, 45° to the beam. Details concerning spectrometer calibration are described in Davis et al.⁵

Short working distance (SWD), miniature X-ray emission spectrometers (miniXES) were used to record Mn *K β* emission. These spectrometers use multiple flat Bragg analyzers to reflect X-ray fluorescence onto a Pilatus 100k (by Dectris) two-dimensional position-sensitive detector (2D-PSD).^{31–34} The miniXES design is based on the observation that a microfocused incident beam permits one to obtain good energy resolution from a flat analyzer crystal that is only a few centimeters from the sample.^{31–34} We utilized two different miniXES configurations suitable for the analysis of Mn *K β* emission. The first instrument uses the Ge 440 reflection in a Johansson arrangement,³⁵ allows for a 100 eV collection range containing the *K β'* , *K β* _{1,3} (emission from the 3p level), and *K β''* peaks, and demonstrates an instrumental energy resolution of $\sim 1.5 \text{ eV}$. To improve the energy resolution, the second design instead uses the GaP 440 reflections in a von Hamos configuration.³⁶ This von Hamos design has a decreased collection range of 50 eV, including only the *K β* main lines. It demonstrates an increased energy resolution of $\sim 0.3 \text{ eV}$ which is comparable to that of spectrometers utilizing spherically bent crystal analyzers (SBCAs).²⁶ More details can be found in Davis et al.⁵

Measurements on the dark-adapted *S*₁ state of PSII were done at room temperature (RT). Undamaged PSII Mn *K β* _{1,3} spectra were obtained, and damage studies were performed. Fresh PSII (protected by a synchronized shutter) was exposed to the full intensity microfocused X-ray beam (e.g., $10^{12} \text{ photons/s}$ at 20-ID). PSD exposures were collected in defined time intervals throughout the irradiation (e.g., the shortest for 20-ID were at $\sim 7 \text{ ms}$). In order to obtain the desired signal-to-noise ratio, multiple images were summed together for different points on the sample corresponding to the same total irradiation period. These divisions allowed us to monitor the X-ray-induced damage over time.

Mathematical Methods. The mathematical model we use to fit the experimental data⁵ consists of a system of ordinary differential equations (ODEs) with respect to time. To account for the considerable thickness of studied PSII samples ($\sim 1 \text{ mm}$) and the effect of attenuation on both the incident X-ray beam and generated fluorescence, we introduce slices of 10 μm , over which we assume constant *r_c* (equal to the number of

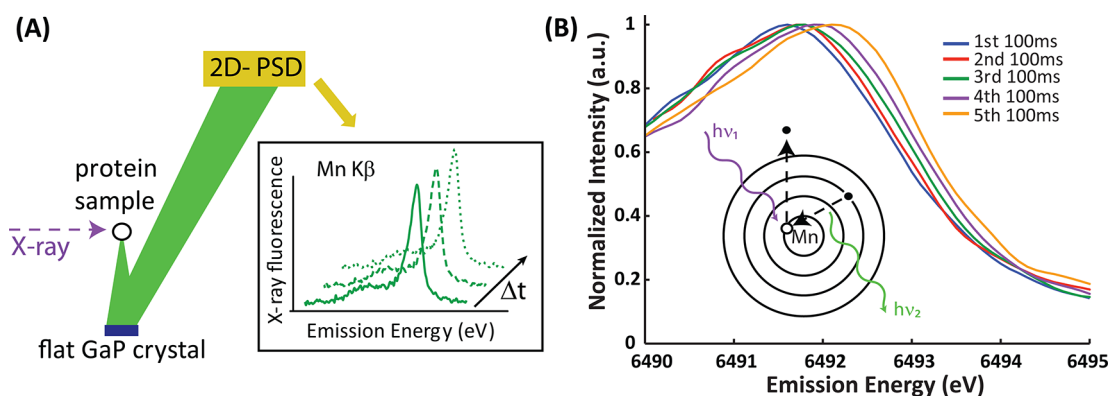


Figure 1. In XES experiments (photon-in-photon-out spectroscopy), the sample is excited with an X-ray photon of sufficient energy to create a 1s hole (above the K-edge absorption energy for Mn in this work). Repopulation of this 1s hole from other energy levels (3p in the case of $K\beta$ emission) results in the emitted X-ray fluorescence which is then analyzed by Bragg reflection from a suitable crystal plane. (A) The X-ray fluorescence is reflected via Bragg scattering from a flat analyzer crystal onto the position-sensitive detector. Pixel-to-energy calibration allows us to reconstruct the XES spectrum. Detector readout is possible for different time intervals indicated as Δt . (B) Effect of the progression of X-ray-induced damage on the Mn $K\beta$ PSII XES spectrum. Data are shown for consecutive 100 ms exposures. The shift of the XES spectrum to higher energy is due to the photoreduction of the OEC containing Mn^{III} and Mn^{IV} ions to Mn^{II} .

radicals created by the photons absorbed in this sample thickness), and solve the system for each $10\ \mu\text{m}$ depth interval. This gives us a set of rates for each step in the “z” direction (into the sample); see eq 1.

$$r_c = (\Phi)(\zeta)(e^{-\alpha z_i}e^{-\alpha z_i} - e^{-\alpha z_{i+1}}) \quad (1)$$

where the first term, Φ , represents the flux per unit volume (e.g., $1.1 \times 10^7\ \text{photons s}^{-1}\ \mu\text{m}^{-3}$) and the second term, ζ , the number of radicals created per absorbed photon (e.g., ~ 190). The first exponential converts the flux to the transmitted flux at any given depth, z_i , given by Beer–Lambert’s law, $I/I_0 = e^{-\alpha z}$, where $\alpha = 1.46 \times 10^{-3}\ \mu\text{m}^{-1}$ in the case of bulk sample approximated as water, and the final term provides the number of photons absorbed in each $10\ \mu\text{m}$ slice. Note that z_1 represents position “zero”, the surface of the sample; it follows that z_{100} is $990\ \mu\text{m}$ into the sample.

We then take a weighted average over those rate values whose individual importance is again determined by Beer–Lambert’s law. This method provides reaction rates (k_1 and k_2) for every $10\ \mu\text{m}$ step into the depth of the sample (fitting by assuming all data points originated in that layer; see Supporting Information, Table S1) as well as “weighted average” values of k_1 and k_2 to simulate the experimental fluorescence data. We apply the same weighting to the calculated Mn^{2+} content, shown in Figure 3 as a solid line.

We employ either MATLAB’s *ode45* or *ode15s* algorithm iteratively in conjunction with the MATLAB function *lsqcurvefit* to fit the experimental data with the proposed model and to find the optimal values for the k_1 and k_2 parameters. *ode45* is a one-step ODE solver utilizing the Dormand–Prince method.³⁷ In order to use this solver, it is necessary to remove the stiffness of the problem by dividing out a factor of 10^6 . *ode15s*, while often less accurate, relies on numerical differentiation formulas and is efficient at solving stiff problems. Our results indicate an equivalency between these two solvers (Figure 3). To fit these data, we run *lsqcurvefit* with appropriate starting values and conditions ($R(t = 0) = 0$ and $[\text{rad}(t = 0)] = 0$) on the numerical solution to eq 5 below. To allow for alternative initial values of $[\text{rad}(t = 0)]$, we predominantly use *ode15s*, unless specified.

RESULTS AND DISCUSSION

Experimental Analysis of X-ray-Induced Damage to PSII. In this work, we monitor the progression of X-ray-induced damage to PSII via Mn $K\beta$ XES. The dispersive nature of the miniXES allows us to collect data with high time resolution (Figure 1A). XES involves the excitation of an inner shell electron into the continuum and subsequent repopulation of the newly created hole (Figure 1B, insert). $K\beta$ emission lines correspond to $3p \rightarrow 1s$ transitions. While the $K\beta$ spectrum is ~ 8 times less intense than $K\alpha$ emission ($2p \rightarrow 1s$ transition), it has higher sensitivity to the electronic structure of the Mn center because of the exchange interaction between the $3p$ and $3d$ orbitals. This interaction creates a multiplet spread of 15 eV from which the doublet ($K\beta'$ and $K\beta_{1,3}$) arises. The position of the more intense $K\beta_{1,3}$ peak is often used to determine changes in oxidation state.^{26,38} As the oxidation state decreases, more electrons are present in the $3d$ level, increasing the valence spin, and leading to a greater exchange interaction (increased splitting) between $3d$ and $3p$. Thus, if considering only the $K\beta_{1,3}$ peak, it appears to shift to higher energies with the reduction of Mn ions. We use this shift to monitor the extent of X-ray-induced photoreduction to the Mn cluster (Figure 1B). Undamaged room-temperature S_1 state XES data were reported previously.⁵ We analyzed the X-ray-induced damage progression by “overexposing” the sample (Figure 1B). Currently, it is accepted that the OEC in the S_1 state contains two Mn^{III} and two Mn^{IV} ions that are all susceptible to reduction to Mn^{II} . This reduction can be monitored by XES and any spectral shift to higher energies. X-ray emission spectra of Mn^{II} solution added into PSII samples were taken to mimic fully damaged S_1 state samples.

Utilizing previously collected undamaged S_1 state XES data, we created calibration spectra composed of a chosen ratio of these data and XES of Mn^{II} in solution. These spectra then served as a comparison to the collected data for determining the percent reduction to Mn^{II} (Figure 2). Comparisons of experimental and calibration spectra were done visually. The difference in the spectrometers (damage studies were done with two different spectrometers, see Figure 2 caption) created spectral shape variations due to differences in energy resolution. To account for uncertainties in the visual determinations of the

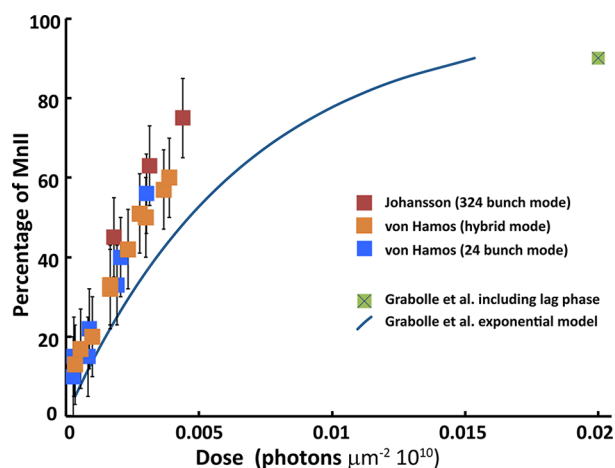


Figure 2. X-ray-induced damage to the OEC expressed as a percentage of Mn^{II} plotted versus photon dose for RT. RT data collected from the Johansson (red, excitation energy 7.5 keV) and von Hamos miniXES (light blue and orange corresponding to different beamtimes, excitation energy 7.09 keV) instruments. The dark blue line was calculated from the data of Grabolle et al.⁶ reporting exponential decay with a rate of damage $k = 0.9 \text{ min}^{-1}$ for RT measurements taken with a flux of $\sim 10^{12} \text{ photons s}^{-1} \text{ mm}^{-2}$ (i.e., $10^6 \text{ photons s}^{-1} \mu\text{m}^{-2}$). This is 100 times less than the flux presented in this paper. Note that they also reported an exposure time of $\sim 200 \text{ s}$ resulting in 90% Mn^{II} (the green point). See Table 1 for more details regarding the fill patterns during the respective data sets.

peak center, we conservatively estimated the error to be $\pm 10\%$ for each point.

For an increased signal-to-noise ratio, we sacrificed time resolution by summing not only all data corresponding to the same irradiation period (usually 20 ms, monochromatic beam, or each $\sim 40 \mu\text{s}$ pulse, pink beam) but also, when reasonable, sets of three (e.g., total of 60 ms) or five (e.g., total of 100 ms) sequential exposure periods. Any spectral shifts occurring in these intervals would be averaged together and could potentially skew the data. In order to correct for this, we approximated the shifts in $K\beta_{1,3}$ as linear for such small time scales. It follows that the damage observed in an averaged set of exposures actually reflects the damage caused by half the dose deposited during that time frame plus the dose deposited in the preceding time interval(s). This assumption is only a reasonable first approximation at very short time scales, comparable with the minimum data collection interval.

We compared our results with the only available PSII room-temperature damage study reported by Grabolle et al.⁶ (Figure 2). Both data sets fall within the same order of magnitude (Figure 2) in spite of the 100 times higher rate of dose deposition used in our study. However, we did not observe the

reported lag phase prior to the onset of damage, which could be attributed to differences in the rate of dose deposition.

Kinetic Modeling of X-ray-Induced Damage at Room Temperature. Earlier RT damage analysis by Grabolle et al. describes the kinetics of damage by a single exponential model with $k_{\text{main}} = 0.9 \text{ min}^{-1}$.⁶ Such a model sheds little light on the mechanism of damage. It is critical to develop a more detailed model that can be used to predict damage under a variety of experimental conditions such as an increased rate of dose deposition, available with pink beam mode at third-generation synchrotrons and new ultrafast high brilliance sources such as the linac coherent light source (LCLS). Depending on the effect of dose deposition rate on the damage profile, it may be possible to collect data prior to the onset of damage even with very intense sources.^{4,19,24}

Unlike in X-ray crystallographic studies detecting X-ray scattering, the generation of X-ray emission requires absorption of the X-rays by samples (the process producing the damage). Because of the low dilution of our target metal ions, it is highly unlikely that direct absorption by Mn and the creation of Auger electrons (less prevalent for heavier elements such as Mn) is the main source of damage. Instead, we hypothesize that absorption into the bulk sample and subsequent radiolysis of water creates radicals whose interaction with the probed species dominates room-temperature X-ray damage in biological samples. We approximate PSII-enriched thylakoid membrane fragments as water for the purposes of X-ray absorption.

In its most general form, the rate equations for a reaction of the OEC with radicals can be written as

$$\frac{d[S_1(t)]}{dt} = k_2[S_1(t)][\text{rad}(t)] \quad (2)$$

and

$$\frac{d[\text{rad}(t)]}{dt} = r_c - r_d - r_r \quad (3)$$

where $[S_1(t)]$ represents the concentration of undamaged Mn (Mn^{IV} and Mn^{III} ions) in the S_1 state of PSII, $[\text{rad}(t)]$ the concentration of radicals, and k_2 the rate constant associated with the radical–Mn ion interaction; r_c , r_d , and r_r represent the rates of radical creation, decay, and interaction with S_1 , respectively. Aqueous electrons, e^-_{aq} , and hydroxyl radicals, OH^\bullet , are the most prevalent and reactive species created through water radiolysis each with a G value (the number of radicals of a particular species created after the deposition of 100 eV of energy into water) of approximately 2.6–2.7.^{39–42} This implies that for every photon with an energy of 7090 eV, about 190 radicals (e^-_{aq} as well as OH^\bullet) are created. However, OH^\bullet is a highly oxidizing species. As the damage in PSII is manifest through the reduction of the Mn_4Ca cluster, we

Table 1. Comprehensive Description of Basic Beam Parameters Including Fill Patterns and Bunch Spacing as Well as the Corresponding Spectrometer Type and Beamline for All Data Presented in Figure 2 and Referenced in Figure 5

#	Data	Fill Pattern	Spacing	Spectrometer	Beamline
1		324 singlets (0.31 mA)	11.37 ns (uniform)	Johansson	20-ID
2		24 singlets (4.25 mA)	153 ns (uniform)	von Hamos	20-ID
3		Hybrid (single 16 mA isolated bunch, 8 groups of 7 11 mA bunches)	(non-uniform) symmetrical 1.594 μs surround 16 mA bunch \rightarrow 51 ns between consecutive 11 mA bunches	von Hamos	20-ID
4		324 singlets (0.31 mA)	11.37 ns (uniform)	von Hamos	14-ID

propose that the effects of the hydroxyl radical are either secondary processes or, with regard to the Mn ions, nondominant. In contrast, aqueous electrons are a highly reducing species, with a high G value similar to that of the OH^\bullet radical.^{39–42}

With a sample thickness of 1 mm, a spot size of $\sim 105 \times 85 \mu\text{m}^2$, and an average flux of 10^{12} photons/s, the absorption by the sample is $8.5 \times 10^4 \text{ photons s}^{-1} \mu\text{m}^{-3}$. Assuming that, as a first approximation, only e^-_{aq} contribute to the damage, we obtain a rate of radical production, $r_c = 1.57 \times 10^7 \text{ radicals s}^{-1} \mu\text{m}^{-3}$ or 26 mM s^{-1} . While this is a reasonable approximation, it averages the effect of attenuation by the sample and does not take into account the uneven distribution of radicals through the sample volume due to the exponential absorption term. Given the short-lived nature of aqueous electrons and consequent limited effect of diffusion, it is more accurate to consider r_c as a function of depth to account for attenuation occurring through the sample. See Materials and Methods for additional details. The rate of radical production (r_c) is independent of the radical concentration and can, thus, be considered zeroth order. However, according to previous studies, the “decay” of e^-_{aq} is a first-order reaction.⁴³

Considering r_r to be the rate of reaction with PSII, we can now rewrite eq 3 as the following:

$$\frac{d[\text{rad}(t)]}{dt} = r_c - k_1[\text{rad}(t)] - k_2[S_1(t)][\text{rad}(t)] \quad (4)$$

where r_c is determined iteratively through the sample thickness and k_1 is the rate constant of e^-_{aq} decay. The solution to this equation must be determined numerically. However, we first combine eqs 2 and 4 analytically to yield

$$\frac{d^2R(t)}{dt^2} + \frac{dR(t)}{dt}(k_1 + Ak_2e^{-k_2R(t)}) - r_c = 0 \quad (5)$$

where $R(t) = \int [\text{rad}(t)] dt$ and $A = [S_1(0)] = (1.5)(3 \times 10^5 \text{ PSII}/\mu\text{m}^3)$ or 0.75 mM . Note that the S_1 state has Mn ions in both the III and IV oxidation states. To account for the presence of the Mn^{IV} ions, which require two electrons to reduce to Mn^{II} , we multiply the initial concentration of undamaged Mn by 1.5. This is a simplification that assumes Mn^{IV} and Mn^{III} ions have similar reduction kinetics. So far, no biexponential kinetics has been reported for the rate of photoreduction for Mn^{III} versus Mn^{IV} ions. This simplification will slightly lower the rate constant (k_2) of Mn reduction by substituting the sequential reduction of Mn^{IV} to Mn^{III} and then to Mn^{II} by introducing instead two Mn ions capable of single-electron reduction.

As shown in Figures 2 and 3, the $[S_1(t)]$ data are most easily displayed as a percentage of Mn^{II} accumulated in the sample. To fit the experimental data, we therefore use the equation

$$\% \text{Mn}^{\text{II}} = 100(1 - e^{-k_2R(t)}) \quad (6)$$

These fits (Figures 3 and 4, Table 2) yield the weighted mean rate constants $k_1 = 4.0 \times 10^7 \text{ s}^{-1}$ and $k_2 = 17.1 \mu\text{m}^3 (\text{number of radicals})^{-1} \text{ s}^{-1}$ at a χ^2 value of ~ 3.2 . Note that this value indicates an overestimation of error (chosen conservatively as $\pm 10\%$) in visually assigning percent damage. Converting to more common units for k_2 , we obtain $k_2 = 1.03 \times 10^{10} \text{ M}^{-1} \text{ s}^{-1}$. When $k_1 = 4.0 \times 10^7 \text{ s}^{-1}$, the lifetime for aqueous electrons is $\tau \sim 2.5 \times 10^{-8} \text{ s}$ in the PSII sample. According to Cercek and Cercek,⁴³ the aqueous electron has a lifetime $\tau \sim 4.5 \times 10^{-8} \text{ s}$

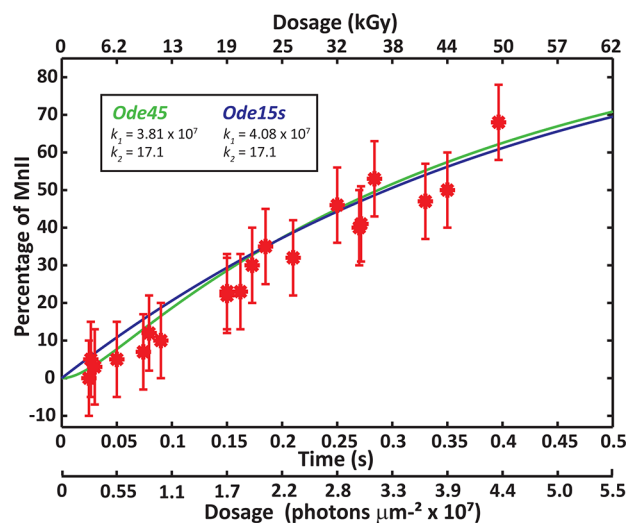


Figure 3. Data presented in Figure 2 fit by the proposed model (green, *ode45*; blue, *ode15s*). All beamtimes were considered a unified data set. Note that the percent error was not taken into account during the fit. Error bars are present to provide a measure of uncertainty in the data, as before.

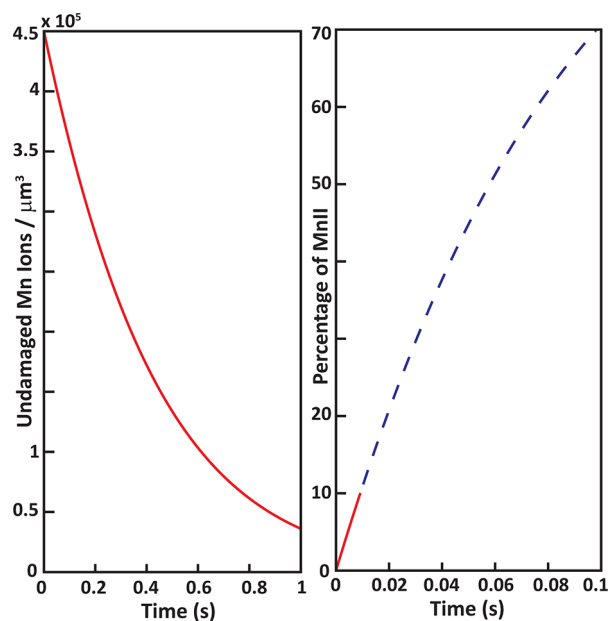


Figure 4. (left panel) Model prediction for the number of undamaged PSII S_1 state centers (number of Mn ions divided by 4) per unit volume as a function of time, given monochromatic beam conditions and ignoring the bunch structure (i.e., “continuous” $\sim 1.1 \times 10^8 \text{ photons s}^{-1} \mu\text{m}^{-2}$). (right panel) Assuming a sample thickness of $10 \mu\text{m}$, a comparison between “continuous” (dashed blue) and “pulsed” (i.e., accounting for bunch structure, solid red) models for a monochromatic beam in 24-bunch mode. See Table 1 for additional details regarding this mode.

in protein-enriched environments at room temperature, lending credibility to model values for k_1 and k_2 .

Up to this point in the modeling, we ignored the time structure of the X-ray beam obtained from $\sim 100 \text{ ps}$ electron bunches with variable spacing (depending on the fill mode of APS, see Table 1). It happens that the data presented in Figure 2 were collected in different fill modes (see Table 1). If we compare the lifetime of aqueous electrons ($\sim 21 \text{ ns}$) with the

Table 2. Values of the Least Squares Fit Using *ode15s*

point	time (ms) ^a	percentage Mn experiment	percentage Mn theory	weighted mean residual
<i>t</i> ₁	24.7	0	0	0
<i>t</i> ₂	26.4	5	0.400	−4.59
<i>t</i> ₃	30.0	3	1.20	−1.79
<i>t</i> ₄	50.0	5	5.62	0.594
<i>t</i> ₅	74.1	7	10.7	3.65
<i>t</i> ₆	79.3	12	11.8	−0.272
<i>t</i> ₇	90.0	10	13.9	3.86
<i>t</i> ₈	150	22	25.2	3.09
<i>t</i> ₉	150	23	25.2	2.10
<i>t</i> ₁₀	162	23	27.3	4.20
<i>t</i> ₁₁	172	30	29.1	−0.970
<i>t</i> ₁₂	185	35	31.1	−3.95
<i>t</i> ₁₃	210	32	35.0	3.00
<i>t</i> ₁₄	250	46	40.9	−5.03
<i>t</i> ₁₅	270	40	43.7	3.70
<i>t</i> ₁₆	271	41	43.9	2.93
<i>t</i> ₁₇	284	53	45.5	−7.40
<i>t</i> ₁₈	330	47	51.2	4.34
<i>t</i> ₁₉	350	50	53.5	3.67
<i>t</i> ₂₀	396	68	58.43	−9.26

^aNote that the values of time were calculated by taking the dosage accumulated and assuming an incident flux of 10^{12} photons/s.

spacing between electron bunches, we see that this lifetime is longer than the X-ray pulse spacing in 324-bunch mode (11.4 ns); however, the ~ 153 ns spacing of the 24-bunch model is longer than the lifetime of solvated electrons. Hybrid fill has a mixed pattern with more complicated dependencies (Table 1). Our experimental results were insensitive to these differences (Figure 2). To verify the simplification of substitution of the pulsed X-ray beam by a continuous one, we compared the predicted damage using values obtained for the rate constants k_1 and k_2 , assuming an incident flux of 10^{12} photons s^{-1} and a beam projection of $\sim 105 \times 85 \mu m^2$ (right panel of Figure 4). Computationally this was done by solving the differential equations for each electron bunch iteratively and compounding the radicals produced. Note that to perform our pulsed beam equivalency tests, we approximate X-ray bunches on the order of picoseconds as non-zero initial radical concentrations ($[rad(t = 0)] \neq 0$ instant radical injection) and set a rate of radical production $r_c = 0$.

Prediction of the Progression of X-ray-Induced Damage for a Variable Rate of Dose Deposition.

Assuming the rate constants (k_1 and k_2) are independent of flux, we can use the model to predict damage progression with different rates of dose deposition. While some previous studies indicate a damage progression independent of dose rate, we propose this is affected by the magnitudes of deposition rates considered. Note the rates we compare, ranging from 126 kGy s^{-1} (monochromatic) to 4500 kGy s^{-1} (pink beam, during the pulse), are much higher than those considered earlier.¹⁷ We consider three typical rates: monochromatic beam, characteristic of ID beamlines at third-generation synchrotron sources; pink beam, produced at ID beamlines without the use of a monochromator; and an X-ray FEL beam, such as the one generated at LCLS. Experimentally, we observed greater than $\sim 6.7 \times 10^6$ to $\sim 1.1 \times 10^7$ photons μm^{-2} (corresponding to 7.6×10^3 to 1.3×10^4 Gy; note that this was calculated using the full sample thickness and an energy of 7.1 keV) as the dosage

limit for 5% damage from ~ 1 mm of sample (monochromatic beam),⁵ while the model calculations for such a thickness indicate a dosage threshold at $\sim 2.5 \times 10^6$ photons μm^{-2} (corresponding to 2.8×10^3 Gy, given the same parameters). We consider these two numbers to be in good agreement. To simplify the modeling for different rates of dose deposition, we compare calculations for a single $10 \mu m$ slice with a $1 \times 1 \mu m^2$ cross section (Table 3). According to the model, the dosages

Table 3. Comparison of Predictions for Damage Progression

facility	rate of dose deposition (photons s^{-1}) ^a	number of photons to 5% damage	dosage in Gy to 5% damage ^a	time to 5% damage
APS monochromator	1×10^{12}	5.0×10^5	5.7×10^4	~ 4.5 ms
APS pink beam	3×10^{15}	5.3×10^5	6.7×10^4	~ 1 μs
LCLS	1×10^{25}	10^9	1.3×10^8	~ 0.55 ps

^aAssuming 7.1 keV for monochromatic beam and 7.85 keV (ignoring undulator spread) for pink and LCLS beams on a $10 \mu m$ thick PSII sample of area $1 \times 1 \mu m^2$ and assuming continuous deposition. Note that for a beam delivered as pulses, the values for dose deposition rate are those calculated for the dosing time only.

required for 5% damage during both pink beam ($\sim 3 \times 10^{15}$ photons s^{-1} , during the pulses) and monochromatic beam ($\sim 10^{12}$ photons s^{-1}) are similar: 5.3×10^5 photons μm^{-2} (corresponding to 6.7×10^4 Gy assuming an incident energy of 7.85 keV and ignoring undulator spread) in pink beam mode and 5.0×10^5 photons μm^{-2} (or 5.7×10^4 Gy) in monochromatic mode, assuming a $10 \mu m$ sample thickness. Thus, in spite of a 3000-fold increase in the rate of dose deposition, the effective damage remains overwhelmingly dependent on the total number of deposited photons.

For heat load management, the pink beam is delivered in the form of microsecond pulses using a rotating high-heat-load shutter. Figure 5 shows the progression of damage as a function of number of X-ray pulses ($\sim 40 \mu s$ /pulse), each of which deposits $\sim 3 \times 10^{11}$ photons. We average the pulses in sets of two in order to increase statistics. This is possible as we do not

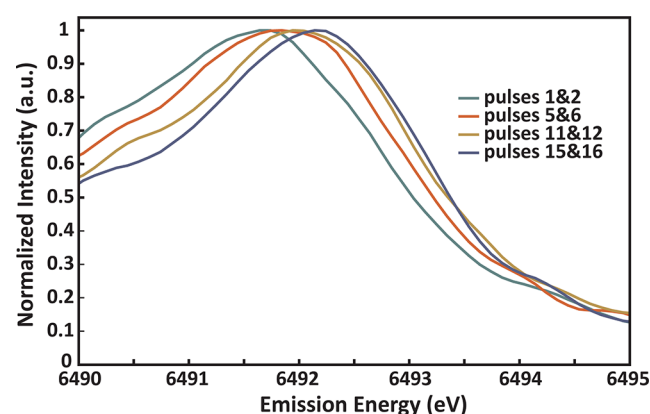


Figure 5. Effect of the progression of X-ray-induced damage on the Mn K β PSII XES spectrum given pulsed ($\sim 40 \mu s$ pulse duration) pink beam exposure. Data are shown in sets of two sequential pulses ($\sim 3 \times 10^{11}$ photons/pulse) averaged for improved statistics. The shift of the XES spectrum to higher energy is due to the photoreduction of the OEC containing Mn^{III} and Mn^{IV} ions to Mn^{II}. We do not see a shift within the first two or three pulses. This indicates a dosage threshold higher than that of the monochromatic beam, experimentally determined to be minimally 6×10^{10} photons.

observe any obvious damage within the first two pulses. Experimentally, we observed $\sim 1.4 \times 10^8$ photons μm^{-2} (corresponding to 1.8×10^5 Gy at 7.85 keV peak undulator energy, and full sample depth) as the upper dose limit for a ~ 1 mm thick sample. This corresponds to a ~ 20 -fold increase in the dosage threshold between monochromatic (threshold minimally $\sim 6.7 \times 10^6$ photons μm^{-2} , or 7.6×10^3 Gy) and pink ($\sim 1.4 \times 10^8$ photons μm^{-2} , or 1.8×10^5 Gy) beams.

The effect appears to be stronger than the one predicted by the model. We propose that the simplicity of our model is responsible for the discrepancies between the pink beam damage threshold measured experimentally and the model prediction. Other radicals and/or processes such as those described above likely affect the concentration of solvated electrons responsible for reduction of the OEC. For instance, recombination between the solvated electrons and OH^\bullet radicals can become significant at higher rates of dose deposition (recombination rate constant, $3.02 \times 10^{10} \text{ M}^{-1} \text{ s}^{-1}$ according to Ryuji et al.⁴⁴). It has been proposed previously that short, high-intensity X-ray pulses could be used to acquire data prior to the onset of damage processes such as those initiated by photoelectrons, Auger electrons, and radiolysis.

Before concluding, we discuss the application of our model to the vastly higher dose rates achievable at new X-ray FEL sources such as the LCLS. According to our model, the exposure time to reach 5% damage in the Mn oxidation state is ~ 1 ps for a single pulse at LCLS (taken as 10^{25} photons s^{-1} during the ~ 100 fs duration of the pulse). This indicates a dose limit of 10^{10} photons μm^{-2} for a $10 \mu\text{m}$ sample thickness (Figure 6). The 1 ps damage time is longer than the 100 fs data

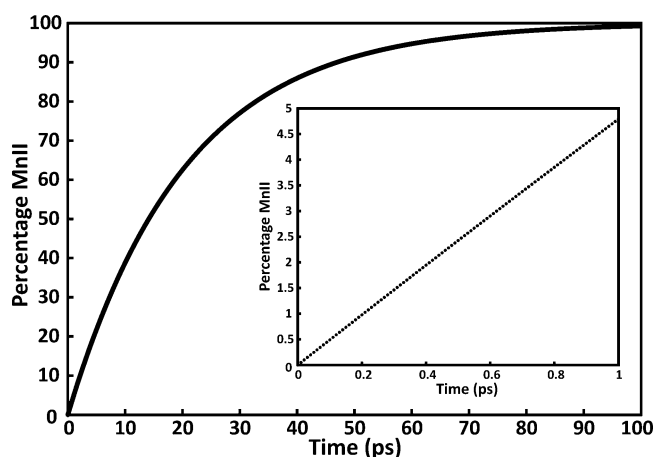


Figure 6. Considering a $10 \mu\text{m}$ slice of sample and a spot size of $10 \times 10 \mu\text{m}^2$, we apply our model of pulsed beam structure for a single pulse at LCLS (10^{12} photons). Note that, as was done with all our pulsed model runs, we assume this dosage is deposited instantaneously at $t = 0$. (Inset) Time to 5% damage given 1 pulse is ~ 1 ps, well after the experimental pulse duration of ~ 100 fs.

collection time, implying that an even higher number of photons can be used within a single LCLS pulse. However, caution should be exercised in case other physical/chemical processes become significant with such ultrahigh rates of dose deposition.^{2,4,45}

Time scales for the LCLS approach those required for the generation of primary electrons (~ 10 fs) as well as those for the generation of solvated electrons ($\sim 10^{-13}$ s).⁴⁴ Thus, at such a source, data might be acquired with the least damage, as

damaging species are created on the time scale of data collection and thus do not have time to chemically interact.²⁵ The factor of $\sim 20\,000$ -fold increase in the deposited dose at LCLS resulting in the same extent of damage is an exciting outcome of the presented model. It suggests that experimentation with higher rates of dose deposition is beneficial for measurements of biological samples sensitive to radiation damage. A few comments must be made here. As pink beam and X-ray FEL sources are typically delivered in the form of pulses (composed of sets of “bunches” inherent to the ring), it is beneficial in the experimental design to create a single pulse delivering the threshold dose (the dose just below the onset of X-ray-induced damage). However, the application of high rates of dose deposition might result in the creation of other radicals or initiation of processes for which the presented model does not account.

■ ASSOCIATED CONTENT

§ Supporting Information

Unweighted values of parameters k_1 and k_2 . This material is available free of charge via the Internet at <http://pubs.acs.org>.

■ AUTHOR INFORMATION

Corresponding Author

*E-mail: ypushkar@purdue.edu.

Notes

The authors declare no competing financial interest.

■ ACKNOWLEDGMENTS

The research at Purdue University was supported by the U.S. Department of Energy (DOE), Office of Basic Energy Sciences DE-FG02-12ER16340 (Y.P.) and the National Science Foundation Graduate Research Fellowship under Grant 0833366 (K.M.D.). Research at the University of Washington is supported by the U.S. DOE, Office of Basic Energy Sciences DE-SC0002194. PNC/XSD facilities at the Advanced Photon Source and research at these facilities are supported by the DOE, Basic Energy Sciences, a Major Resources Support grant from NSERC, the University of Washington, Simon Fraser University, and the Advanced Photon Source. Use of the Advanced Photon Source, an Office of Science User Facility operated for the DOE Office of Science by Argonne National Laboratory, was supported by the U.S. DOE under Contract DE-AC02-06CH11357. Use of the BioCARS Sector 14 was also supported by grants from the National Center for Research Resources (5P41RR007707) and the National Institute of General Medical Sciences (8P41GM103543) from the National Institutes of Health (NIH). The time-resolved setup at BioCARS was funded in part through a collaboration with Philip Anfinrud (NIH/National Institute of Diabetes and Digestive and Kidney Diseases). We acknowledge the help of beamline personnel Dr. Steve Heald, Dr. Dale Brewster, and Dr. Tim Graber in conducting XES measurements. We also thank Vatsal Purohit for help with PSII preparations.

■ REFERENCES

- (1) Graber, T.; Anderson, S.; Brewer, H.; Chen, Y. S.; Cho, H. S.; Dashdorj, N.; Henning, R. W.; Kosheleva, I.; Macha, G.; Meron, M.; et al. BioCARS: A Synchrotron Resource for Time-Resolved X-ray Science. *J. Synchrotron Radiat.* **2011**, *18*, 658–670.
- (2) Chapman, H. N.; Fromme, P.; Barty, A.; White, T. A.; Kirian, R. A.; Aquila, A.; Hunter, M. S.; Schulz, J.; DePonte, D. P.; Weierstall, U.;

et al. Femtosecond X-ray Protein Nanocrystallography. *Nature* **2011**, *470*, 73–77.

(3) Hunter, M. S.; Fromme, P. Toward Structure Determination Using Membrane-Protein Nanocrystals and Microcrystals. *Methods* **2011**, *55*, 387–404.

(4) Lomb, L.; Barends, T. R. M.; Kassemeyer, S.; Aquila, A.; Epp, S. W.; Erk, B.; Foucar, L.; Hartmann, R.; Rudek, B.; Rolles, D.; et al. Radiation Damage in Protein Serial Femtosecond Crystallography Using an X-ray Free-Electron Laser. *Phys. Rev. B* **2011**, *84*, 214111–214111-6.

(5) Davis, K. M.; Mattern, B. A.; Pacold, J. I.; Zakharova, T.; Brew, D.; Kosheleva, I.; Henning, R. W.; Graber, T. J.; Heald, S. M.; Seidler, G. T.; et al. Fast Detection Allowing Analysis of Metalloprotein Electronic Structure by X-ray Emission Spectroscopy at Room Temperature. *J. Phys. Chem. Lett.* **2012**, *3*, 1858–1864.

(6) Grabolle, M.; Haumann, M.; Muller, C.; Liebisch, P.; Dau, H. Rapid Loss of Structural Motifs in the Manganese Complex of Oxygenic Photosynthesis by X-ray Irradiation at 10–300 K. *J. Biol. Chem.* **2006**, *281*, 4580–4588.

(7) Yano, J.; Yachandra, V. K. Where Water Is Oxidized to Dioxygen: Structure of the Photosynthetic Mn_4Ca Cluster from X-ray Spectroscopy. *Inorg. Chem.* **2008**, *47*, 1711–1726.

(8) Yano, J.; Kern, J.; Irrgang, K.-D.; Latimer, M. J.; Bergmann, U.; Glatzel, P.; Pushkar, Y.; Biesiadka, J.; Loll, B.; Sauer, K.; et al. X-ray Damage to the Mn_4Ca Complex in Photosystem II Crystals: A Case Study for Metallo-Protein X-ray Crystallography. *Proc. Natl. Acad. Sci. U.S.A.* **2005**, *102*, 12047–12052.

(9) Ziaja, B.; London, R. A.; Hajdu, J. Unified Model of Secondary Electron Cascades in Diamond. *J. Appl. Phys.* **2005**, *97*, 064905–1–064905-9.

(10) Stern, E. A.; Yacoby, Y.; Seidler, G. T.; Nagle, K. P.; Prange, M. P.; Sorini, A. P.; Rehr, J. J.; Joachimiak, A. Reducing Radiation Damage in Macromolecular Crystals at Synchrotron Sources. *Acta Crystallogr., Sect. D: Biol. Crystallogr.* **2009**, *65*, 366–374.

(11) Barker, A. I.; Southworth-Davies, R. J.; Paithankar, K. S.; Carmichael, I.; Garman, E. F. Room-Temperature Scavengers for Macromolecular Crystallography: Increased Lifetimes and Modified Dose Dependence of the Intensity Decay. *J. Synchrotron Radiat.* **2009**, *16*, 205–216.

(12) De la Mora, E.; Carmichael, I.; Garman, E. F. Effective Scavenging at Cryotemperatures: Further Increasing the Dose Tolerance of Protein Crystals. *J. Synchrotron Radiat.* **2011**, *18*, 346–357.

(13) Sanishvili, R.; Yoder, D. W.; Pothineni, S. B.; Rosenbaum, G.; Xu, S. L.; Vogt, S.; Stepanova, S.; Makarov, O. A.; Corcoran, S.; Benn, R.; et al. Radiation Damage in Protein Crystals Is Reduced with a Micron-Sized X-ray Beam. *Proc. Natl. Acad. Sci. U.S.A.* **2011**, *108*, 6127–6132.

(14) Warkentin, M.; Badeau, R.; Hopkins, J.; Thorne, R. E. Dark Progression Reveals Slow Timescales for Radiation Damage between $T = 180$ and 240 K. *Acta Crystallogr., Sect. D: Biol. Crystallogr.* **2011**, *67*, 792–803.

(15) Meents, A.; Gutmann, S.; Wagner, A.; Schulze-Bries, C. Origin and Temperature Dependence of Radiation Damage in Biological Samples at Cryogenic Temperatures. *Proc. Natl. Acad. Sci. U.S.A.* **2010**, *107*, 1094–1099.

(16) Swarts, S. G.; Gilbert, D. C.; Sharma, K. K.; Razskazovskiy, Y.; Purkayastha, S.; Naumenko, K. A.; Bernhard, W. A. Mechanisms of Direct Radiation Damage in DNA, Based on a Study of the Yields of Base Damage, Deoxyribose Damage, and Trapped Radicals in $\text{D}(\text{Gcacgcgtgc})(2)$. *Radiat. Res.* **2007**, *168*, 367–381.

(17) Owen, R. L.; Yorke, B. A.; Gowdy, J. A.; Pearson, A. R. Revealing Low-Dose Radiation Damage Using Single-Crystal Spectroscopy. *J. Synchrotron Radiat.* **2011**, *18*, 367–373.

(18) Beitlich, T.; Kuhn, K.; Schulze-Bries, C.; Shoeman, R. L.; Schlichting, I. Cryoradiolytic Reduction of Crystalline Heme Proteins: Analysis by UV-Vis Spectroscopy and X-ray Crystallography. *J. Synchrotron Radiat.* **2007**, *14*, 11–23.

(19) Aquila, A.; Hunter, M. S.; Doak, R. B.; Kirian, R. A.; Fromme, P.; White, T. A.; Andreasson, J.; Arnlund, D.; Bajt, S.; Barends, T. R. M.; et al. Time-Resolved Protein Nanocrystallography Using an X-ray Free-Electron Laser. *Opt. Express* **2012**, *20*, 2706–2716.

(20) Haumann, M.; Muller, C.; Liebisch, P.; Iuzzolino, L.; Dittmer, J.; Grabolle, M.; Neisius, T.; Meyer-Klaucke, W.; Dau, H. Structural and Oxidation State Changes of the Photosystem II Manganese Complex in Four Transitions of the Water Oxidation Cycle ($\text{S}_0 \rightarrow \text{S}_1$, $\text{S}_1 \rightarrow \text{S}_2$, $\text{S}_2 \rightarrow \text{S}_3$, and $\text{S}_{3,4} \rightarrow \text{S}_0$) Characterized by X-ray Absorption Spectroscopy at 20 K and Room Temperature. *Biochemistry* **2005**, *44*, 1894–1908.

(21) Haumann, M.; Grabolle, M.; Neisius, T.; Dau, H. The First Room-Temperature X-ray Absorption Spectra of Higher Oxidation States of the Tetra-Manganese Complex of Photosystem II. *FEBS Lett.* **2002**, *512*, 116–120.

(22) Haumann, M.; Pospisil, P.; Grabolle, M.; Muller, C.; Liebisch, P.; Sole, V. A.; Neisius, T.; Dittmer, J.; Iuzzolino, L.; Dau, H. First Steps Towards Time-Resolved BioXAS at Room Temperature: State Transitions of the Manganese Complex of Oxygenic Photosynthesis. *J. Synchrotron Radiat.* **2002**, *9*, 304–308.

(23) Haumann, M.; Liebisch, P.; Muller, C.; Barra, M.; Grabolle, M.; Dau, H. Photosynthetic O_2 Formation Tracked by Time-Resolved X-ray Experiments. *Science* **2005**, *310*, 1019–1021.

(24) Schmidt, M.; Srajer, V.; Purwar, N.; Tripathi, S. The Kinetic Dose Limit in Room-Temperature Time-Resolved Macromolecular Crystallography. *J. Synchrotron Radiat.* **2012**, *19*, 264–273.

(25) Alonso-Mori, R.; Kern, J.; Gildea, R. J.; Sokaras, D.; Weng, T. C.; Lassalle-Kaiser, B.; Tran, R.; Hattne, J.; Laksmono, H.; Hellmich, J.; et al. Energy-Dispersive X-ray Emission Spectroscopy Using an X-ray Free-Electron Laser in a Shot-by-Shot Mode. *Proc. Natl. Acad. Sci. U.S.A.* **2012**, *109*, 19103–19107.

(26) Messinger, J.; Robblee, J. H.; Bergmann, U.; Fernandez, C.; Glatzel, P.; Visser, H.; Cinco, R. M.; McFarlane, K. L.; Bellacchio, E.; Pizarro, S. A.; et al. Absence of Mn-Centered Oxidation in the S_2 to S_3 Transition: Implications for the Mechanism of Photosynthetic Water Oxidation. *J. Am. Chem. Soc.* **2001**, *123*, 7804–7820.

(27) Umena, Y.; Kawakami, K.; Shen, J. R.; Kamiya, N. Crystal Structure of Oxygen-Evolving Photosystem II at a Resolution of 1.9 Å. *Nature* **2011**, *473*, 55–U65.

(28) Liang, W.; Roelofs, T. A.; Cinco, R. M.; Rempel, A.; Latimer, M. J.; Yu, W. O.; Sauer, K.; Klein, M. P.; Yachandra, V. K. Structural Change of the Mn Cluster During the $\text{S}_2 \rightarrow \text{S}_3$ State Transition of the Oxygen-Evolving Complex of Photosystem II. Does It Reflect the Onset of Water/Substrate Oxidation? Determination by Mn X-ray Absorption Spectroscopy. *J. Am. Chem. Soc.* **2000**, *122*, 3399–3412.

(29) Rutherford, A. W. Orientation of Electron-Paramagnetic-Resonance Signals Arising from Components in Photosystem-II Membranes. *Biochim. Biophys. Acta* **1985**, *807*, 189–201.

(30) Berthold, D. A.; Babcock, G. T.; Yocum, C. F. A Highly Resolved, Oxygen-Evolving Photosystem II Preparation from Spinach Thylakoid Membranes. EPR and Electron-Transport Properties. *FEBS Lett.* **1981**, *134*, 231–234.

(31) Mattern, B. A.; Seidler, G. T.; Haave, M.; Pacold, J. I.; Gordon, R. A.; Planillo, J.; Quintana, J.; Rusthoven, B. A Plastic Miniature X-ray Emission Spectrometer Based on the Cylindrical von Hamos Geometry. *Rev. Sci. Instrum.* **2012**, *83*, 023901-1–023901-9.

(32) Seidler, G. Short Working Distance Spectrometer and Associated Devices, Systems, and Methods. U.S. Patent 2011/0058652 A1, 2011.

(33) Dickinson, B.; Seidler, G. T.; Webb, Z. W.; Bradley, J. A.; Nagle, K. P.; Heald, S. M.; Gordon, R. A.; Chou, I. M. A Short Working Distance Multiple Crystal X-ray Spectrometer. *Rev. Sci. Instrum.* **2008**, *79*, 123112-1–123112-8.

(34) Pacold, J. I.; Bradley, J. A.; Mattern, B. A.; Lipp, M. J.; Seidler, G. T.; Chow, P.; Xiao, Y.; Rod, E.; Rusthoven, B.; Quintana, J. A Miniature X-ray Emission Spectrometer (MiniXES) for High-Pressure Studies in a Diamond Anvil Cell. *J. Synchrotron Radiat.* **2012**, *19*, 245–251.

- (35) Johansson, T. New Focusing X-ray Spectrometer. *Z. Phys.* **1933**, *82*, 507–528.
- (36) von Hamos, L. Roetgen Spectra Image by Means of the Crystal Effect. *Ann. Phys. (Berlin, Ger.)* **1933**, *17*, 716–724.
- (37) MATLAB, 7.12.0 (R2011a); The MathWorks Inc.: Natick, MA, 2011.
- (38) Glatzel, P.; Bergmann, U. High Resolution 1s Core Hole X-ray Spectroscopy in 3d Transition Metal Complexes—Electronic and Structural Information. *Coord. Chem. Rev.* **2005**, *249*, 65–95.
- (39) *Nuclear Hydrogen Production Handbook*; Yan, X. L., Hino, R., Eds.; CRC Press: Boca Raton, FL, 2011.
- (40) Buxton, G. V.; Greenstock, C. L.; Helman, W. P.; Ross, A. B. Critical Review of Rate Constants for Reactions of Hydrated Electrons, Hydrogen Atoms and Hydroxyl Radicals ($\bullet\text{OH}/\bullet\text{O}^-$) in Aqueous Solution. *J. Phys. Chem. Ref. Data* **1988**, *17*, 513–886.
- (41) Laverne, J. A.; Pimblott, S. M. Diffusion-Kinetic Modeling of the Electron Radiolysis of Water at Elevated Temperatures. *J. Phys. Chem.* **1993**, *97*, 3291–3297.
- (42) Alpen, E. L. *Radiation Biophysics*; Prentice Hall, 1990.
- (43) Cercek, B.; Cercek, L. Pulse-Radiolysis Study of a Biological Matrix. *Int. J. Radiat. Biol.* **1973**, *24*, 137–142.
- (44) Ryuji, N.; Yuta, K. Radiolysis of Water. In *Nuclear Hydrogen Production Handbook*; Yan, X. L., Hino, R., Eds.; CRC Press: Boca Raton, FL, 2011; pp 177–187.
- (45) Neutze, R.; Wouts, R.; van der Spoel, D.; Weckert, E.; Hajdu, J. Potential for Biomolecular Imaging with Femtosecond X-ray Pulses. *Nature* **2000**, *406*, 752–757.